High-resolution far-infrared imaging enabled by 100-kW-peak-power parametric source at 5.7 THz

Like x-ray imaging, THz imaging will require high power and high resolution to advance relevant applications. Previously demonstrated THz imaging usually suffered from one or several difficulties among low power, poor spectral tunability, or limited resolution from a low-frequency source. A radiation source in the 5-10 THz is relatively scarce. Although a short wavelength benefits imaging resolution, widely used imaging sensors, such as microbolometers, Schottky diodes, and photoconductive antennas, are usually not sensitive to radiation with frequencies above 5 THz. The radiation power of a high-frequency source becomes a key factor to realize low-noise, high-resolution imaging by using an ordinary pyroelectric detector. Here, we report a successful development of a fully coherent, tunable, >100-kW-peak-power parametric source at 5.7 THz. It is then used together with a low-cost pyroelectric detector for demonstrating high-resolution imaging in comparison with the same image at 2 THz. To take advantage of the tunable coherent source, we also report spectrally resolved imaging between 5.55~5.87 THz to reveal the spectroscopic characteristics of a test drug, Aprovel, with spatial information.

■ 郭倉禾、吳明雄、黃衍介

Keywords: THz parametric source, THz imaging, Nonlinear optics, Non-destructive detection

1. Origin of research

The origin of the research is based on our development of high-power high-frequency THz parametric sources in the past 10 years or so. THz radiation has the advantage of seeing through a number of important materials and is therefore for non-invasive diagnostics or measurements. The high power enables a better signal-to-noise ratio and the high frequency benefits a high spatial resolution for imaging. Recently, we successfully applied the unique radiation source to measure small features in materials and, for the first time to the best of our knowledge, generated high-resolution spectral images in the far-infrared spectrum.

THz radiation is known to penetrate several materials, such as plastics, polymers, and semiconductors, some of which are opaque to optical radiation. THz wave can also induce resonant absorption in large molecules in complex materials. As a result, THz imaging has become a powerful means to reveal hidden objects with high contrast in some materials [1,2], which is similar to X-ray imaging. This has been exploited in applications, such as security checking [3,4], semiconductor quality assurance [5], and others. In particular, tunable THz radiation is useful for wavelength-sensitive applications such as spectrally resolved imaging for illicit drugs6 and biomedical materials [7,8]. Currently, most THz imaging is performed with a source frequency below 2 THz [3,5,6,8], where commercial microbolometer sensors, Schottky diodes, or photoconductive antennas are available for detection and image construction [9-11]. The demonstrated THz imaging usually suffered from one or several difficulties among low power, poor spectral tunability, or limited resolution from a low-frequency source. A radiation source in the [5-10] THz is relatively scarce. Although a short wavelength benefits imaging resolution, widely used imaging sensors, such as microbolometers, Schottky diodes, and photoconductive antennas, are usually not sensitive to radiation with frequencies above 5 THz. The radiation power of a high-frequency source becomes a key factor in realizing low-noise, high-resolution imaging by using an ordinary pyroelectric detector. To be able to compete with x-ray imaging in systems, the THz source power, and its image resolution would still require a major upgrade. Our research addresses all the important issues associated with high-resolution THz imaging.

2. Research purpose

High source power is important to achieving enough signal-to-noise ratio for imaging, whereas the resolution of an image is scaled by the wavelength of the source illuminating the object. Although high-frequency THz radiation is advantageous for high-resolution imaging, low-cost image sensor arrays are not widely available in the 5–10 THz frequency range. On the other hand, bulk THz sensors, such as pyroelectric detectors and Golay cells, which could be used in this frequency range, usually require an input energy of nJ–μJ to overcome the intrinsic background noise for detection. Therefore, it is worth developing a high-power high-frequency THz source for THz imaging.

Here, we develop a compact, high-power, tunable THz laser source at about 6 THz by using KTP. Then, we demonstrate the feasibility of using it for high-resolution THz imaging by using an economic pyroelectric detector. This device and the demonstrated results open up potential impacts on non-invasive diagnostics for semiconductor and biomedical materials.

Method

1.Unique THz Source.

The coherent THz radiation is generated from the SPS in KTP [12-14] and lithium niobite [15-17]. An SPS process is the same as a parametric amplification process, except that SPS involves an enhanced parametric gain and absorption loss from Raman-like vibration of the material lattice. The peak SPS gains for KTP and lithium niobate are located at 5.7 and 2 THz, respectively. **Figure 1** shows the schematic of our two-stage KTP parametric source for demonstrating the high- resolution THz imaging. The system is pumped by a sub-ns Nd:YAG laser amplifier at 1064 nm. The first stage is a KTP PA seeded by a tunable diode laser, generating a high-power red-shifted Stokes pulse. The second stage is a DFG for the pump and Stokes pulses, producing a high-power THz pulse via SPS in the 2nd KTP crystal. A silicon prism is used to couple out the THz radiation from the 2nd KTP crystal for imaging experiments. Our system was optimized to generate as much THz power as possible from KTP. For SPS with high absorption at THz, the THz output is determined from the competition between the parametric gain coefficient Γ and the material absorption coefficient α_{THz}, where Γ^2 is proportional to the pump intensity. For KTP, $\alpha_{THz} = 252\ cm^{-1}$ at 5.7 THz, which is significantly larger than the maximum parametric gain coefficient $\Gamma = 15\ cm^{-1}$ attainable at the maximum pump intensity of our laser system. In such a high-absorption and low-gain limit, the growth of the THz power PTHz is governed by the expression [18]

$$P_{THz}(L) = P_s \frac{\omega_{THz}}{\omega_s}\left(\frac{2\Gamma}{\alpha_{THz}}\right)^2 (1-e^{-\alpha_{THz}L/2})^2, \quad (1)$$

where P_s is the power of the Stokes wave, ω is the angular frequency of the wave, and L is the crystal length. In our system, we first generate a pulsed P_s from a PA and inject it into a downstream DFG to generate P_{THz} according to **Eq. (1).** In our system, the PA and DFG are pumped by a single 120-mJ pulsed laser at 1064 nm. The pump pulse rate is 10 Hz. Assume that the total available power from the pump laser P_0 is split into two parts, rP_0 for pumping the PA and $(1-r)P_0$ for pumping the DFG, where r is the power splitting ratio. The THz power in **Eq. (1)** is then proportional to the multiplication of the Stokes and pump powers in the DFG or

$$P_{THz}(L) \propto P_s P_p = \eta_s r P_0 \times (1-r) P_0 , \quad (2)$$

where η_s is the conversion efficiency for the PA and is typically saturated at ~ 15% at pump depletion [19]. The THz power in (2) is maximized when r = 50%. However, in our experiment, we chose to deliver more pump energy the PA to achieve the saturated efficiency. Specifically, a 70-mJ pump pulse is first injected into the PA to generate a ~10-mJ Stokes pulse, which is then mixed with the remaining 50-mJ pump pulse in the THz DFG to generate the highest THz output power.

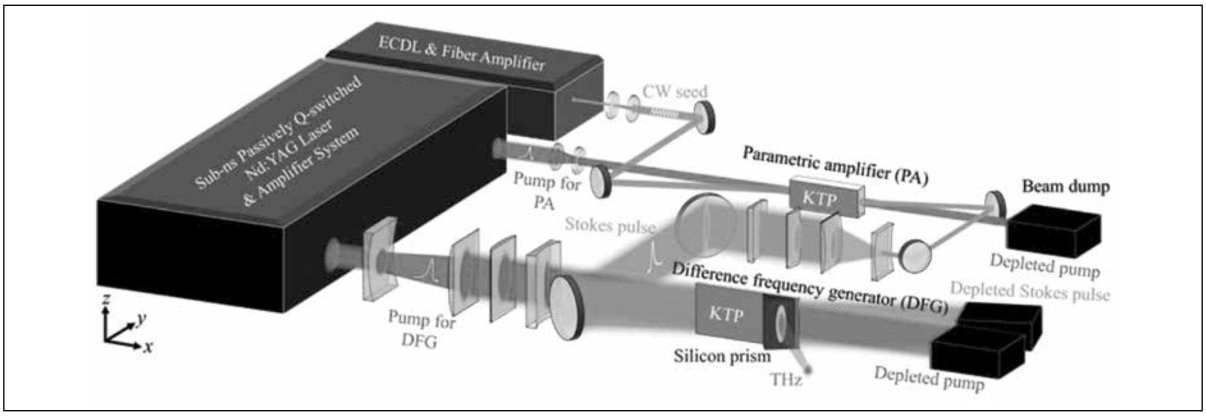

Figure 1. The schematic of the two-stage parametric source for demonstrating the high-resolution THz imaging. The first stage is a KTP PA seeded by a tunable diode laser, generating a high-power Stokes pulse. The second stage is a DFG for the pump and Stokes pulses, producing a high-power THz pulse via SPS in the second KTP crystal.

2.Shadow-image Measurement

Figure 2 shows the experimental setup for performing the shadow- imaging scan. The THz output is first collimated and focused to a focal point on a sample by a set of off-axis parabolic mirrors. The same PA-DFG system was installed with KTP and lithium niobate crystals to generate high-power 5.7- and 2-THz radiations for imaging, respectively. While transversely scanning the sample relative to the THz beam, we record the transmittance of the THz wave by using the THZ5I-BL-BNC detector behind the sample. The responsivity of the THZ5I-BL- BNC is 23 times better than the THz-20 detector. The sensor size of the detector is 5×5 mm, which is placed at 5 cm behind the sample. Although the 2-THz output has a lower available peak power of about 6 kW, the signal-to-noise ratio of the detector was well over 100 during the measurements for a typical noise floor of ~1 mV for an ordinary oscilloscope. For each pixel data in the image, we used the built-in circuit of the oscilloscope to average 8 signal pulses from the incident THz wave. Since the transmission of the THz wave through the sample is normalized to the incident power, and the numerical aperture of the two imaging systems remains the same for all the experiments, the scanned shadow images can give a reliable comparison of the wavelength dependence of the image resolution for the same leaf sample.

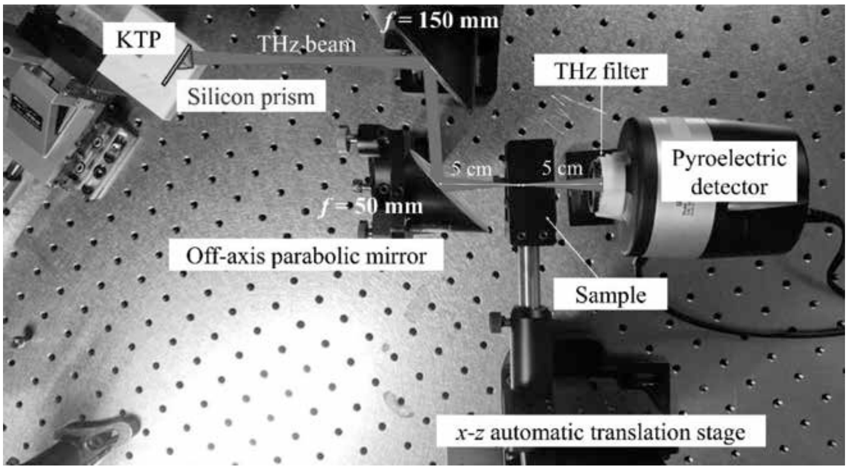

Figure 2. The experimental setup for performing scanning shadow imaging, wherein the THz wave is focused to the sample and the transmittance of it is recorded by a bulk pyroelectric detector

To estimate the resolution of the THz source, we measured the numerical aperture with the knife-edge measurement and imaging of a 3D-printed USAF-1951. Assume the THz radiation has a Gaussian beam profile. The normalized THz power P(x) from knife-edge measurement is given by $P(x) = 0.5\times\left\{1\text{- erf}\left[\left(a\times x - x_0\right)/\left(w_0/\sqrt{2}\right)\right]\right\}$, where a is the fitting factor, x is the position of the knife, and w_0 is the beam radius. When a = 0.9893, x_0 = 0.63, and w_0 = 0.3, the estimated beam radius was 0.3 mm by fitting the differentiated P(x) curve as shown in **Fig. 3**. The numerical aperture (NA) of a Gaussian beam radiation is given by NA = n × sin (θ) ≈ $\lambda/(\pi w_0)$, where n is the refractive index, θ is the divergent angle of the beam, and λ is the radiation wavelength. The calculated NA is equal to 0.055 at 52 μm. According to the definition of resolution R = (1.22 × λ)/ (2 × NA), the calculated resolution of 5.7 THz imaging is about 570 μm. To estimate the value of the imaging resolution, we prepared the USAF- 1951 electric file and printed it out by using a 3D printer (Zortrax Inkspire) as shown in **Fig. 4(a,b)**. The substrate of the 3D-printed USAF-1951 is UV curable resin. Its thickness is 1 mm and the dimension is 3.4 × 3.4 cm. As shown in **Fig. 4(c)**, the slit with a width narrower than 500 μm was resolved.

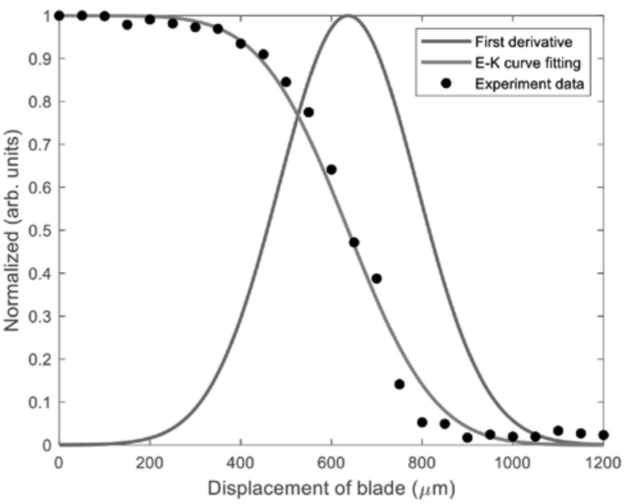

Figure 3. Knife-edge measurement of 5.7 THz radiation. The red line is the fitting curve based on the cumulative distribution function of Gaussian. The blue line is the differential curve of the red line, indicating the beam radius of 300 μm.

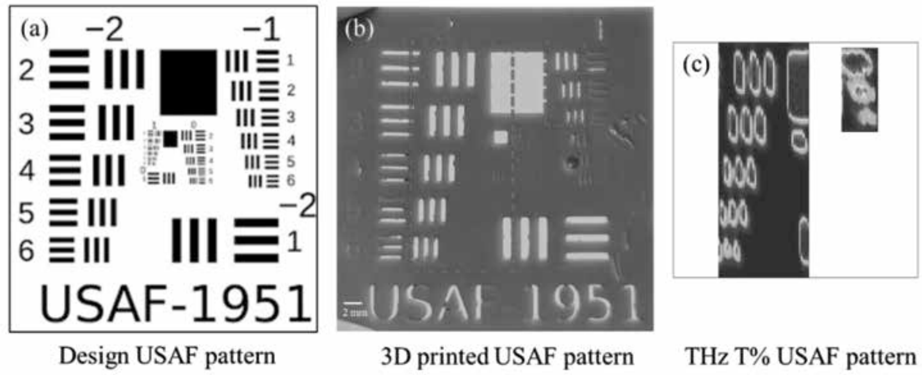

Figure 4. (a) The figure of a USAF-1951 electric file. (b) The optical photo of the USAF-1951 sample, we made by a 3D printer. (c) The 5.7 THz imaging of the 3D-printed USAF-1951 sample The THz imaging can resolve the width of <500 μm on the 3D-printed USAF-1951 sample

3. Sample Preparation.

The leaf was first freshly picked from a tree (Alternanthera bettzickiana (Regel) Nicholson)) and was embedded between two polyethylene films by using a commercial laminator. The thickness of the polyethylene film is 170 μm. The average transmittance of the leaf for the incidence wave at 5.7 THz increases from almost zero to about 40% when the color of the leaf slowly turns gray due to the loss of its water content. Once the THz transmittance of the leaf sample saturates at a fixed value, the same sample is used throughout the imaging experiments. To perform spectral imaging, we first ground a few drugs, including Aprovel, LerZanidip, Aspirin, and Caffeine, and carefully distributed each kind of the powder into a 3 × 3 mm square area on a polyethylene film. We then covered the powders by using another polyethylene film and used the same laminator to fix the powders for transmittance measurements between 5.55 and 5.90 THz. We found that the THz transmittance curve of Aprovel has a relatively large variation in the frequency band of the measurement. We then proceeded with the spectral-imaging experiments for the 3 × 3 mm area of Aprovel to generate the images.

Result and Discussion

1. High-power THz Source.

KTP is highly absorptive at THz frequencies. To maximize the THz output, it is desirable to perform difference-frequency generation in KTP and quickly couple out the THz wave. **Figure 5** shows the two primary parts of our high-power THz parametric system using KTP as the gain crystal. The first part in **Fig. 5a** is a pulse-pumped parametric amplifier (PA) for generating a narrow-line red-shifted laser from a single-longitudinal-mode pump wave at 1064 nm. The red-shifted pulse, called the Stokes or signal pulse, is then injected into the second part of the system **(Fig. 5b)**, which is a difference-frequency generator (DFG) producing a high-power THz pulse at the difference frequency of a pump pulse and the Stokes pulse. The pump pulses for both the PA and DFG are split from an amplified passively Q-switched Nd:YAG laser pulse with a single longitudinal mode and a 450-ps pulse width. The Nd:YAG laser system is capable of delivering more than 120- mJ pulse energy to the downstream PA and DFG. The seed for the PA is a continuous-wave (CW) external-cavity diode laser (ECDL) followed by a fiber laser amplifier. The ECDL is tunable between 1060 and 1090 nm, having a sub-MHz linewidth.

The fiber laser amplifier boosts the ECDL seed power from a few mW up to 0.6 W. The nonlinear materials for the PA and THz DFG are optically polished uncoated KTP crystals, having dimensions of 30(x) × 6(y) × 12(z) and 35(x) × 1(y) × 25(z) mm, respectively. To have a high-energy throughput, the pump laser in the PA has an elliptical beam profile with radii of 2.1(y) × 2.8(z) mm along the minor and major axes, respectively. The signal-laser profile in the PA is circular, having a 2.8-mm radius to fully cover the elliptical pump beam and reduce amplified parametric fluorescence. In the THz DFG, both the pump and Stokes beam profiles are elliptical, having radii of 0.5(y) × 11.1(z) and 0.5(y) × 18(z) mm along the minor and major axes at the crystal center, respectively. The Stokes beam is again arranged to enclose the pump beam to avoid broadband optical parametric generation from the strong pump. The output beam profile of the THz radiation is therefore the overlapping area of the pump and Stokes beams in the DFG crystal. The thin crystal dimension along y permits off-axis oscillation for the THz wave and thus higher parametric efficiency for the SPS [20]. To utilize the largest nonlinear susceptibility d_{33} of KTP, all the mixing waves are polarized along the crystallographic z direction of KTP. A high-resistivity silicon prism is attached to the y-surface of the DFG KTP crystal to couple out the THz wave. A low-pass filter (LPF) with a cutoff wavelength at 20 μm is used to block the pump and Stokes from entering the pyroelectric detector at the output of the prism coupler.

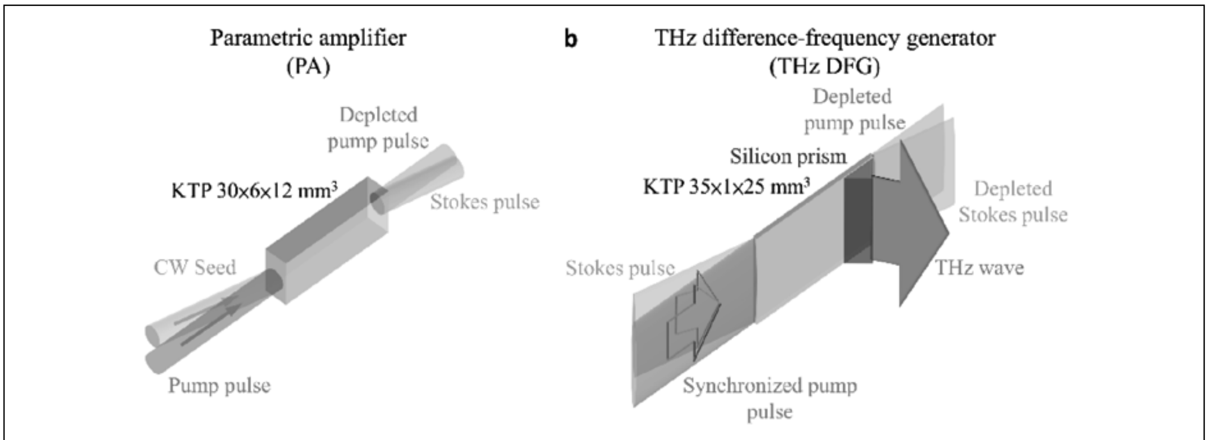

Figure 5. Schematic of the high-power THz parametric source using KTP as the gain crystal. The system consists of (a) a parametric amplifier (PA) for generating a strong Stokes pulse and (b) a subsequent difference frequency generator (DFG) for mixing the pump and Stokes pulses to generate high-power THz radiation. The pump pulses are generated by an amplified, passively Q-switched, single-longitudinal-mode laser at 1064 nm

In our experiment, we carefully verified the measured THz output energy by using two calibrated pyroelectric detectors, including one from SLT Sensor with responsivity of 0.175 V/μJ (THz-20) and the other from Gentec with responsivity of 4.03 V/μJ (THZ5I-BL-BNC) [21]. **Figure 6a** shows the maximum THz signal recorded by the THz-20 detector, when the pump and Stokes energy were 50 and 10 mJ, respectively, in the THz DFG. The transmittance of the low-pass filter in front of the pyroelectric detector is 28.6 % at 5.7 THz. The peak signal amplitude of 420 mV in **Fig. 6a** therefore corresponds to a THz pulse energy of 8.4 μJ/pulse. The responsivity of the THZ5I-BL-BNC detector is about 23 times better and the same THz signal gave a peak amplitude of 9.7 V in the same measurement.

It is necessary to know the width of the THz pulse to determine the THz peak power. Since both the pump and Stokes waves are single-longitudinal-mode in the THz DFG, the generated THz wave is expected to have a transform-limited linewidth. To measure the THz wavelength, we first built a scanning Fabry-Perot spectrometer consisting of two reflecting plates made of high- resistivity silicon. **Figure 6b** shows the interference fringes of the THz pulse scanned by the Fabry-Perot spectrometer with a step size of 1 μm. The periodicity of the interference fringes confirms a 52-μm wavelength of the signal at 5.77 THz. To measure the THz pulse width, we further built a Michelson interferometer with a silicon beam splitter to measure the interferogram of the output THz pulse. The THz pulse width can be deduced from the envelope width of the interferogram. To avoid energy jitter over a long scan time, we did not intend to resolve individual fringes of the interferogram, but simply performed a coarse scan for the envelope by using a step size of 100 μm. **Figure 6c** shows the scanned envelope data fit by the autocorrelation of two Gaussian pulses with a wavelength of 52 μm and a pulse width of 83 ps. The Fabry-Perot spectrometer gives a better signal-to-noise ratio, because the data taking time is much shorter for just a few fringes. By using the 83-ps pulse width for the THz output, **Fig. 6d** plots the THz output energy (left vertical axis) and peak power (right vertical axis) versus pump energy. For this plot, the Stokes energy seeding into the THz DFG is fixed at 10 mJ. As can be seen from the figure, the maximum THz peak power emitted from the silicon prism exceeds 100 kW. Given the refractive index of 3.4 for silicon, the Fresnel loss on the air-side surface of the silicon prism is 30 %. Internal to the silicon output coupler, the peak power of the THz radiation is estimated to be 142 kW, which could be mostly coupled out by using an anti-reflection layer atop the silicon [17]. The data in **Fig. 6d** does not show any obvious saturation even at the highest pump energy. Therefore, it is possible to further scale up the THz output power by increasing the pump and Stokes energy.

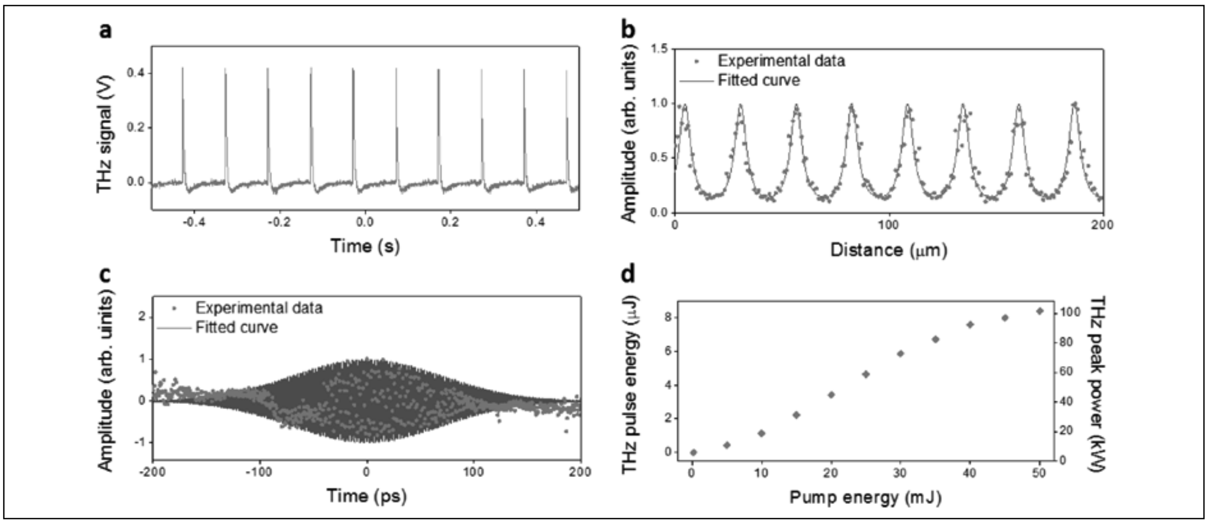

Figure 6. The maximum THz-pulse signal detected by our pyroelectric detector (THz-20, SLT Sensor) when the Stokes energy and pump energy are 10 and 50 mJ in the DFG crystal, respectively. The corresponding THz pulse energy is 8.4 μJ. (b) Interference fringes scanned by a Fabry-Perot interferometer, indicating a THz wavelength of 52 μm. (c) Coarsely scanned Michaelson interferogram of the THz pulse fit by the autocorrelation of two Gaussian pulses with a wavelength of 52 μm, indicating a THz pulse width of 83 ps. (d) THz output energy (left vertical axis) and peak power (right vertical axis) versus pump energy. The Stokes pulse energy seeding into the THz DFG is fixed at 10 mJ. With the 83-ps pulse width deduced from (b), the maximum THz peak power detected by the pyroelectric detector is 100 kW

To compare, we list in **Table 1** a few parameters between this work and two previously demonstrated high-power multi-cycle THz parametric sources using KTP. In 2020, Jia et al. reported the generation of 17-μJ pulse energy at 5.7 THz from KTP by using 580-mJ pump energy in a 7.5-ns width and 36.6-mJ Stokes energy [22]. If, similar to our case, the THz pulse width is approximately 5 times reduced from the pump or 1.5 ns, the corresponding THz peak power is 11.3 kW. Rubidium- doped KTP is often used for fabricating periodically poled KTP (PPKTP) for quasi-phase-matched nonlinear wavelength conversion [23]. In 2021, Tian *et* al. demonstrated the generation of 0.72-μJ output energy at 0.5 THz with a 3-GHz linewidth from a cryogenically cooled PPKTP by using a multi-line pump laser at about 1030 nm. Assuming a transform-limited pulse width for the 0.5-THz pulse, the corresponding THz peak power is about 5 kW. Refer to Methods. Our source is optimized to maximize the THz output power. The much higher peak power generated from this work benefits to applications requiring a high THz field.

Table 1. Comparison between multi-cycle THz parametric sources using KTP

	This work	Jia *et al.* [22]	Tian *et al.* [23]
Material	KTP	KTP	Rb:PPKTP
Frequency	5.7 THz	5.7 THz	0.5 THz
Temperate	room	room	77 K
THz pulse energy (μJ)	8.4	17	0.72
THz peak power (kW)	101.2	11.3*	4.9**

*Assuming one-fifth of the pump pulse width. ** Assuming a transform limited pulse of 147 ps, although the pump pulse width is 250 ps.

2. High-resolution THz Imaging

Imaging can be a power- or energy-demanding process, because the radiation signal collected on an image sensor is only a percentage of the total incident signal that is reflected from or transmitted through a sample. The excellent signal-to-noise ratio presented in **Fig. 6a** is promising for imaging using an ordinary bulk pyrodetector as a single-pixel detector. As a test, we mounted the THZ5I-BL-BNC pyroelectric detector on an x-z scanning stage to measure the THz beam profile through a 0.5-mm diameter aperture on the THz detector. **Figure 7** shows the measured transverse profiles of the THz wave at different locations from the output of the silicon coupler. The scanning step, i.e., the pixel size, of the images is 250 μm. As can be seen from the images at 23, 30, 35 mm from the prism coupler, the THz beam is well collimated in x and focused in z, having a circular beam profile with a ~1 mm rms diameter at 35 mm from the prism.

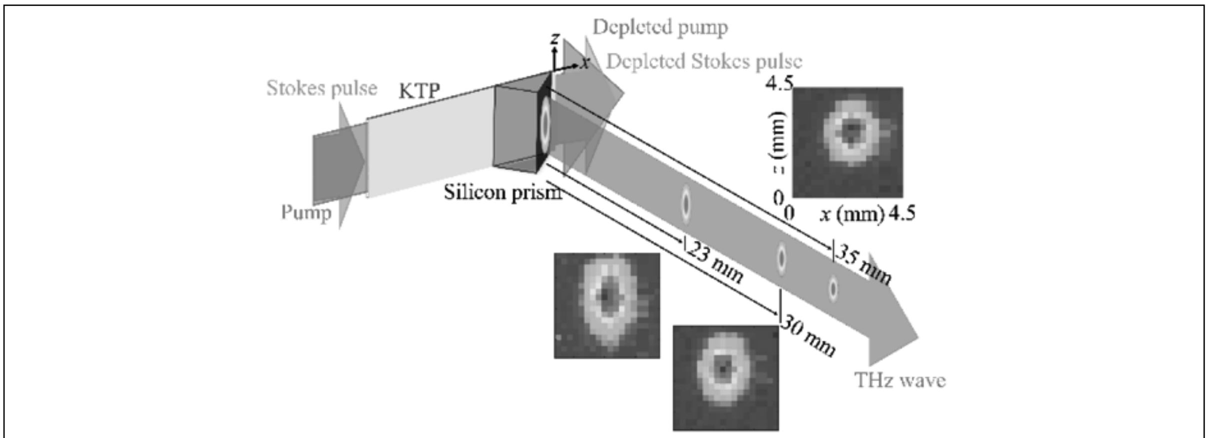

Figure 7. Scanning images of the 5.7-THz beam profile at 23, 30, 35 mm from the output of the silicon prism. The scanning step or the pixel size for the images is 250 μm. The THz beam is collimated in x and focused in z before the 35-mm location

In principle, the diffraction-limited resolution of an image is scaled by the wavelength of the light incident on the object. When compared with an ordinary source with a frequency below 2 THz, our ~6-THz source is expected to give 3-time better resolution for imaging. To compare, by using the same PA-DFG system, we replaced the KTP crystals with lithium niobate crystals to generate high- power radiation at 2 THz and performed an imaging test under the same experimental conditions. The ECDL wavelength was tuned to 1071 nm to match that of the Stokes pulse for lithium niobate in this case. The ultimate resolution of an imaging system is related to both the wavelength of the source and the numerical aperture of the system. In this comparison, we do not strive to build an imaging system with the highest resolution subject to a particular radiation wavelength, but intend to compare the quality of the images generated from the same imaging system with the 5.7 THz and 2 THz sources. Such a relative comparison avoids uncertainties from imaging systems with different numerical apertures.

The sample for imaging comparison at 5.7 and 2 THz is a leaf (Alternanthera bettzickiana (Regel) Nicholson)). **Figure 8a** shows the optical image of the leaf with its major and minor axes approximately equal to 25 and 20 mm, respectively. **Figure 8b** and **8c** show the shadow images of the full leaf scanned by the focused 5.7 and 2 THz sources, respectively. The scanning step size or the pixel size is 250 μm. It is evident that the 5.7-THz image in **Fig. 8b** is much sharper than the 2- THz one in **Fig. 8c**. In particular, the primary veins of the leaf are clearly seen in **Fig. 8b**, but barely show up in **Fig. 8c**. To further improve the image quality, we continued to scan a small portion of the leaf with a 100-μm step size by using the 2 and 5.7 THz sources. **Figures 8d-f** show the optical, 5.7- THz, and 2-THz images of the boxed area of the leaf in **Fig. 8a**, respectively. The 5.7-THz image in **Fig. 8e** reveals the fine features of the veins and a tear at the right bottom corner of the leaf. On the contrary, the quality of the 2-THz image in **Fig. 8f** has little improvements, because the pixel size is already smaller than the imaging wavelength.

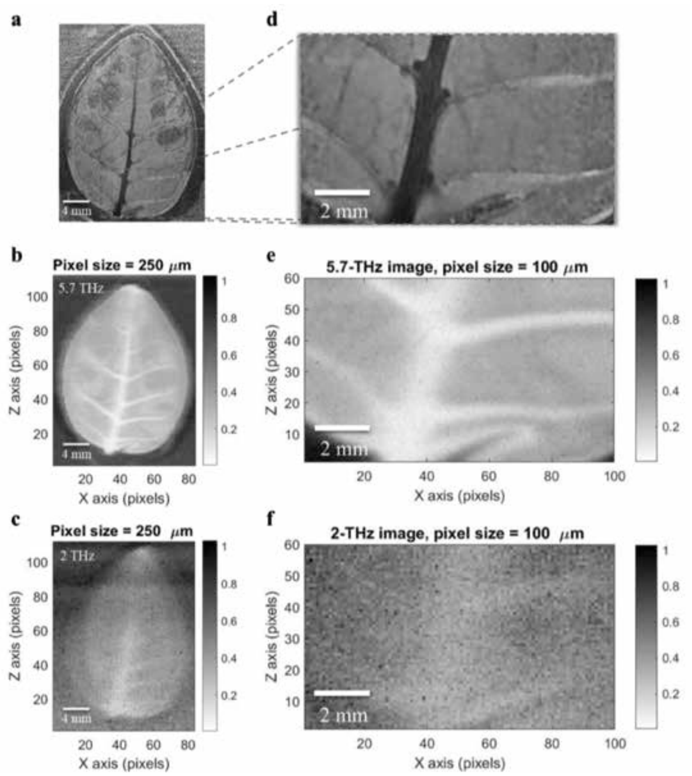

Figure 8. **A dry leaf imaged at visible, ~5.7 THz, and ~2 THz.** (a) Optical image of a leaf embedded between two polyethylene films. (b) 5.7-THz leaf image scanned with a step size of 250μm. (c) 2-THz leaf image scanned with a step size of 250 μm. (d) Enlarged optical image of the leaf for the box area in (a). (e) 5.7-THz image of the boxed leaf scanned with a step size of 100 μm. (c) 2-THz image of the boxed leaf scanned with a step size of 100 μm. The resolution of the 5.7-THz images is apparently better.

3. Spectral Imaging

A major advantage of the THz parametric source is its wavelength tunability. Popular THz parametric sources based on lithium niobate have two primary SPS gain peaks at 2 and 4.2 THz1 [5,24], which limit the frequency tuning range to below 5 THz [25]. The angular bandwidth of the THz SPS in KTP can be a few hundred GHz. By varying the wavelength of the seeding ECDL, it becomes straightforward to tune the frequency of the KTP DFG between 5.5-5.9 THz. To demonstrate a spectrally resolved image, we select a popular drug for blood-pressure control, called Aprovel, as a test chemical. We first spread a small amount of Aprovel powder between two polyethylene films and measured its transmittance curve between 5.55 and 5.87 THz, as shown in **Fig. 9**. The tendency of the transmittance curve matches reasonably well to the known curve in the literature.

We then performed shadow imaging of it using the same imaging scanning system with a 250-μm pixel size at 4 frequencies, 5.61, 5.67, 5.73, 5.79 THz, and compared them (insets) with the characteristic transmittance curve. It is seen in Fig. 9 that the spectral images are indeed correlated with the variation of the transmittance curve. For instance, the image at 5.67 THz shows more transmission than the image at 5.7 THz. The false-color map also reveals the uneven distribution of the powders spread over an area of 3×3 mm (refer to the optical image in the inset). This experiment illustrates an opportunity for spectrally resolved imaging at high THz frequencies by using a tunable high-power coherent THz source and a bulk pyroelectric detector.

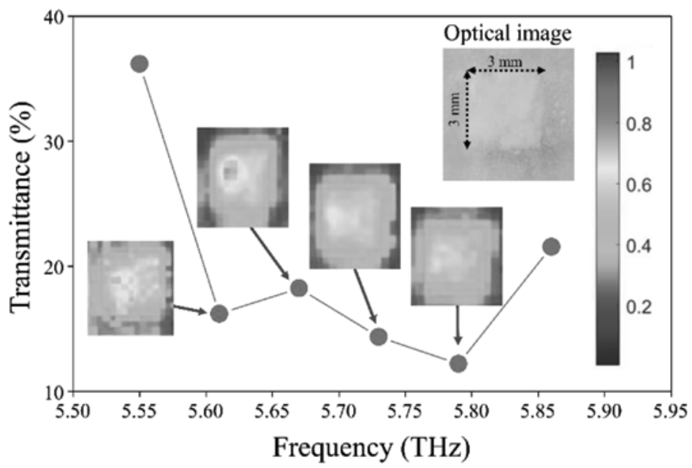

Figure 9. **Spectral imaging of Aprovel powders.** The characteristic transmittance curve of Aprovel powders between 5.55 and 5.87 THz. Insets: (false color) The THz transmittance images of the Aprovel powders between two polyethylene films scanned at 5.61, 5.67, 5.73, 5.79 THz, showing more transmission at 5.67 THz and less transmission at 5.79 THz over a spread area of 3×3 mm for the powders. (gray color) The optical image of the Aprovel sample between two polyethylene films

Conclusion

TIn conclusion, we have developed an ultra-high-power, tunable, coherent, far-infrared radiation source at 5.7 THz based on pulsed difference frequency generation of two single-longitudinal-mode lasers in a thin KTP crystal. The measured maximum peak powers, external and internal to the silicon- prism output coupler atop the KTP DFG are 101 and 142 kW, respectively. The high peak power enables high-resolution scanning imaging at high THz frequencies by using a low-cost pyroelectric detector as a single-pixel image sensor. By using a leaf as a test sample, we show superior shadow images of it at 5.7 THz in comparison with those measured at 2 THz, under the same experimental conditions. By taking advantage of the wavelength tuning capability of the KTP high-power parametric source, we further demonstrated spectrally resolved images of a popular blood-pressure-control drug, called Aprovel, over a spread area of 3×3 mm. The experiment shows the potential to identify the spectroscopic content and the spatial distribution of chemicals using our tunable high- power and high-frequency THz source in conjunction with an ordinary pyroelectric detector.

References

1. Mittleman, D. M., Jacobsen, R. H. & Nuss, M. C. (1996). T-Ray Imaging. EEE J. Sel. Top. Quantum Electron. **2**, 679–692.
2. Duling, I. & Zimdars, D. (2009). Revealing hidden defects. Nat. Photonics **3**, 630–632.
3. Liu, H.-B., Zhong, H., Karpowicz, N., Chen, Y. & Zhang, X.-C. (2007). Terahertz Spectroscopy and Imaging for Defense and Security Applications. Proc. IEEE **95**, 1514–1527.
4. Leahy-Hoppa, M. R., Fitch, M. J. & Osiander, R. (2009). Terahertz spectroscopy techniques for explosives detection. Anal. Bioanal. Chem. **395**, 247–257.
5. True, J., Xi, C., Jessurun, N., Ahi, K. & Asadizanjani, N. (2021). Review of THz-based semiconductor assurance. Opt. Eng. **60**, 060901.
6. Kawase, K., Ogawa, Y., Watanabe, Y. & Inoue, H. (2003). Non-destructive terahertz imaging of illicit drugs using spectral fingerprints. Opt. Express **11**, 2549–2554.
7. Löffler, T. et al. (2001). Terahertz dark-field imaging of biomedical tissue. Opt. Express **9**, 616– 621.
8. Schirmer, M. et al. (2010). Biomedical applications of a real-time terahertz color scanner. Biomed. Opt. Express **1**, 354–366.
9. Mittleman, D. M. (2018). Twenty years of terahertz imaging [Invited]. Opt. Express **26**, 9417– 9431.
10. Dhillon, S. S. et al. (2017). The 2017 terahertz science and technology roadmap. J. Phys. D Appl. Phys. **50**, 043001.
11. Valusis, G., Lisauskas, A., Yuan, H., Knap, W. & Roskos, H. G. (2021). Roadmap of Terahertz Imaging 2021. Sensors **21**, 4092.
12. Wang, W. et al. (2014). Terahertz parametric oscillator based on KTiOPO4 crystal. Opt. Lett. **39**, 3706–3709.
13. Yan, C. et al. (2016). Green laser induced terahertz tuning range expanding in KTiOPO4 terahertz parametric oscillator. Appl. Phys. Lett. **108**, 011107.
14. Wang, Y. et al. (2018). Energy scaling and extended tunability of a ring cavity terahertz parametric oscillator based on KTiOPO4 crystal. Chin. Phys. B **27**, 114213.
15. Hayashi, S. et al. (2014). Ultrabright continuously tunable terahertz-wave generation at room temperature. Sci. Rep. **4**, 5045.
16. Ortega, T. A., Pask, H. M., Spence, D. J., & Lee, A. J., (2017). THz polariton laser using an intracavity Mg:$LiNbO_3$ crystal with protective Teflon coating. Opt. Express **25**, 3991–3999.
17. Tang, L. et al. (2019). Injection pulse-seeded terahertz-wave parametric generator with gain enhancement in wide frequency range. Opt. Express. **27**, 22808–22818.
18. Wang, T.-D. et al. (2013). Long-range parametric amplification of THz wave with absorption loss exceeding parametric gain. Opt. Express **21**, 2452–2462.
19. Chiang, A.-C. et al. (2004). Pulsed Optical Parametric Generation, Amplification, and Oscillation in Monolithic Periodically Poled Lithium Niobate Crystals. IEEE J. Quantum Electron. **40**, 791–799.
20. Chiu, Y.-C., Wang, T.-D., Wang, P.-C. & and Huang, Y.-C. (2019). Off-axis terahertz parametric oscillator. J. Opt. Soc. Am. B **36**, 42–47.
21. The manufacturer of the detector, Gentec-EO, provided us a responsibility value of 0.387 V/μJ in 2018, but corrected it to 4.31~4.66 V/μJ after we reported our own calibration of 4.03 V/μJ to it in 2020.
22. Jia, C. et al. (2020). Theoretical and experimental study on a large energy potassium titanyl phosphate terahertz parametric source. Opt. Laser Technol. **121**, 105817.

23.Tian, W. et al. (2021). μJ-level multi-cycle terahertz generation in a periodically poled Rb:KTP crystal. Opt. Lett. **46**, 741–744.

24.Chiu, Y.-C., Wang, T.-D., Zhao, G. & Huang, Y.-C. (2017). Discovery of high-gain stimulated polariton scattering near 4 THz from lithium niobate. Opt. Lett. **42**, 4897–4900.

25.Murate, K., Hayashi, S. & Kawase, K. (2016). Expansion of the tuning range of injection-seeded terahertz-wave parametric generator up to 5 THz. Appl. Phys. Express **9**, 082401.

26.Sasaki, T. et al. THz Spectral Database for Pharmaceuticals. https://www.rie.shizuoka.ac.jp/~thz/shizuoka_univ_sasaki_lab_database/absorption_pdf_data_ API/Irbesartan_THz_20wtP.pdf

作者簡介

郭倉禾 / 國立清華大學 光電工程研究所

吳明雄 / 國立清華大學 光電工程研究所

黃衍介 / 國立清華大學 光電工程研究所 / 指導老師